Supporting information for

Observation of the Carbon Elimination Channel in Vacuum Ultraviolet Photodissociation of OCS

Wentao Chen[1#], Liang Zhang[1#], Daofu Yuan[1], Yao Chang[1,2], Shengrui Yu[3], Siwen Wang[1], Tao Wang[4], Bin Jiang[1*], Kaijun Yuan[2*], Xueming Yang[2,4], Xingan Wang[1*]

1) Hefei National Laboratory for Physical Sciences at the Microscale and Department of Chemical Physics, University of Science and Technology of China, Hefei, 230026, China
2) State Key Laboratory of Molecular Reaction Dynamics, Dalian Institute of Chemical Physics, Chinese Academy of Sciences, Dalian, 116023, China
3) Hangzhou Institute of Advanced Studies, Zhejiang Normal University, Hangzhou, 311231, China
4) Department of Chemistry, School of Science，Southern University of Science and Technology, Shenzhen, 518055, China

*) Authors to whom correspondence should be addressed:

bjiangch@ustc.edu.cn, kjyuan@dicp.ac.cn, xawang@ustc.edu.cn

#) These authors contributed equally in this work

Experimental methods

The experiments were carried out using a time-sliced velocity map ion imaging (VMI) experimental setup which has been described in detail previously[1-4]. The experimental schematic diagram is shown in Figure S1 which contains the molecular beam, laser and detection system. Briefly, a pulsed supersonic molecular beam of 5% OCS seeded in Ar was expanded into the source chamber by a pulsed valve (General valve, Parker Series 9) with a 1 mm orifice traveling along the central axis of the VMI apparatus. The pulsed valve worked at 20 Hz at a backing pressure of 1 bar. The resulting OCS molecular beam was collimated by a 1.5 mm skimmer before entering the detection chamber. The pulsed and skimmed molecular beam was passed through a 2 mm hole in the first electrode plate of the ion optics and was intersected vertically by the photolysis and probe laser beams between the second and the third electrode plates of the ion optics.

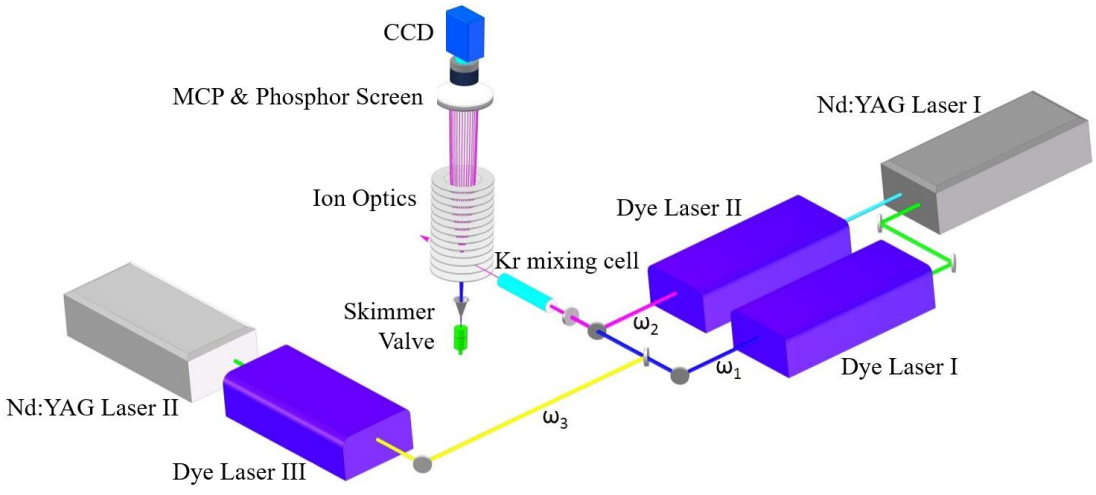

Figure S1. Scheme of the experimental setup.

Two VUV laser beams were employed in this experiment, one for dissociating the

OCS molecules and the other for ionizing the atomic carbon products. As shown in Figure S1, a 212.55 nm (ω_1) laser beam with a typical power of ~ 1.5 mJ/pulse was generated by frequency doubling the fundamental output from dye laser 1 (Sirah Cobra-Stretch). A second tunable visible light (ω_2) with a typical energy of ~ 4 mJ/pulse was provided by dye laser 2 (Sirah Cobra-Stretch). Both dye lasers were pumped by the Nd:YAG Laser 1 (Continuum Powerlite 9020). The two laser beams were spatially and temporally overlapped and focused into a stainless steel cell filled with Kr by using a 30 cm focal length lens. The pressure of Kr was 5~15 Torr in the cell and was adjusted to obtain an optimized signal at different VUV wavelengths. The generated VUV ($2\omega_1$-ω_2) radiation and the residual incident laser light were collimated by an MgF_2 lens and entered the detection chamber. This VUV laser radiation was employed as photolysis laser beam, and its polarization direction was parallel to the detector plane.

The state selective ionization of C($^3P_{J=0}$) products was realized by a VUV (1+1′) resonance-enhanced multiphoton ionization (REMPI) scheme via the intermediate state C*[$2s^2 2p 4s(^3P_J)$].[5] A third dye laser (Sirah Cobra-Stretch) output (ω_3) with a typical energy of ~ 4 mJ/pulse was generated with the pump of a second Nd: YAG laser (Continuum Powerlite 9020), and was used for producing the detection VUV laser beam ($2\omega_1$-ω_3) in the same gas cell as the photolysis VUV radiation. The wavelength of ω_3 was set to be 626.4 nm. The residual UV and visible lights (ω_1, ω_2 and ω_3) served as the second photon to ionize the C atom products. The polarization of the detection laser was perpendicular to the plane of the imaging detector. Doppler scanning of ω_3 was performed for the C($^3P_{J=0}$) fragments to realize the equal detection efficiency of

products with different velocities.

After being accelerated by the ion optics and passing through a 650-mm long time-of-flight tube, the atomic carbon ions were detected by a pair of 70 mm-diameter chevron double micro-channel plates (MCP) coupled with a P43 phosphor screen using the time-sliced VMI method. The transient images on the phosphor screen were recorded by a charge-coupled device (CCD) camera (Imager pro plus 2M, LaVision). A 30 ns gate pulse voltage was applied to the MCP to acquire the time sliced images. The timing of pulsed molecular beam, firing of photolysis and probe lasers, and detector gate pulse was controlled by two delay generators (DG 645, Stanford Research System).

law of energy conservation in photodissociation

The total kinetic energy release (TKER) distributions can be described by the following equation:

$$E\,(\mathrm{TKER}) = E_{h\nu} - D_0 - E_{\mathrm{int}}(\mathrm{SO}) - E_{\mathrm{int}}(\mathrm{C})$$

where $E_{h\nu}$ is the photon energy, D_0 is the threshold energy of the SO($X\ ^3\Sigma^-$) + C($^3P_{J=0}$) channel, E_{int} (SO) is the internal energy of SO($X\ ^3\Sigma^-$) products, and E_{int} (C) is the internal energy of C products determined by excitation of its electronic state.

Computational Details

All electronic structure calculations were performed with the MOLPRO suite of programs.[6] The potential energies were calculated by the internally contracted multi reference configuration interaction (ic-MRCI) method[7,8] based on state averaged complete active space self-consistent field (SA-CASSCF) wavefunctions.[9,10] Davidson

correction (+Q) was applied to approximately account for contributions of higher excitations and improve the size-consistency.[11] Because valance and Rydberg characters are strongly mixed in these high-lying states above ~8 eV or so, we have to use a very large active space that includes multiple virtual orbitals and diffuse functions in the basis set.

Specifically, the cc-pVTZ-F12 basis set of Peterson and co-workers[12] plus extra 3s1p3d diffuse orbitals was employed. The electronic configuration of ground state OCS ($X\,^1\Sigma^+$) at equilibrium geometry can be represented as follows,[13]

$$(core)^{14}(6\sigma)^2(7\sigma)^2(8\sigma)^2(9\sigma)^2(2\pi)^4(3\pi)^4(4\pi)^0(10\sigma)^0(11\sigma)^0\ldots$$

For describing low-lying electronic states, an active space including orbitals from 6σ to 11σ yielding 16 electrons in 12 active orbitals is sufficient, as applied in the previous works.[14,15] However, it is found here that the inclusion of more unoccupied orbitals in the active space is essential to locate the correct states with dominant Rydberg features in the energy range of 8-10 eV. Otherwise, some energy levels are missing. As a result, the active space is selected so as to describe the SO + C dissociation channel,

$$\left[(3\pi)^4(4\pi)^0(10\sigma)^0(5\pi)^0(11\sigma)^0(12\sigma)^0(13\sigma)^0(1\delta)^0\right],$$

with 4 electrons in 11 orbitals to account for those dominant transitions from 3π to unoccupied valence and Rydberg orbitals. Note that more inner σ and π orbitals have to be closed to make the computations feasible. When we compute the CO + S and CS + O channels, however, the inner 9σ orbital has to be included in the active space, without which the CO($^3\Pi$) + S (^3P) products are absent. The active space is

alternatively chosen as,

$\left[(9\sigma)^2(3\pi)^4(4\pi)^0(10\sigma)^0(5\pi)^0(11\sigma)^0(12\sigma)^0(13\sigma)^0\right]$.

To calculate vertical excitation energies, CASSCF wavefunctions were averaged over the six lowest $^1A_1$, $^1B_1$, $^1B_2$, and $^1A_2$ states in C_{2v} symmetry, corresponding to the Abelian point group imposed in MOLPRO to describe the linear OCS belonging to $C_{\infty v}$ symmetry. While in C_s symmetry, the state-averaged CASSCF orbitals were averaged over twelve A' and twelve A" states. The transition dipole moments of the ground single state to excited triplet states were calculated by including spin-orbit (SO) interaction in the Breit-Pauli representation[16] as implemented in MOLPRO. The SO interaction splits each zero-order triplet state into three components with quantum numbers $m_s = 0$ and ± 1, which mixes the triplet and singlet states with the same electronic angular momentum thus making transitions allowed. The sum over the three TDMs of the individual SO states for each triplet state was considered as, $|\mu| = \sum_{m_s}\left(\mu^2_{m_s,x} + \mu^2_{m_s,y} + \mu^2_{m_s,z}\right)^{1/2}$. In what follows all energies are scaled with respect to the minimum of the electronic ground state.

Additional theoretical results

Figure S2 displays relevant molecular orbitals that contribute to the electronic transitions of high-lying electronic states. The character of each orbital at the equilibrium geometry has been analyzed as follows,

9σ: σ_{CS} bonding orbital, with a minor contribution of CO σ bonding orbital,

3π: π_{CS} bonding orbital and the 2p orbital on O,

4π : π^*_{CO} antibonding orbital with the 3p orbital on S,

10σ : $4s\sigma$ Rydberg orbital mainly consisting of 4s orbital on S,

5π : $4p\pi$ Rydberg orbital with contributions from isolated $4p_x/p_y$ orbital on S and $3p_x/p_y$ orbital on O,

11σ : σ^*_{CS} antibonding orbital, with a minor contribution of CO σ bonding orbital,

12σ : a mix of $4s\sigma$ Rydberg orbital with σ^*_{CS} and σ^*_{CO} antibonding orbitals,

13σ : $4p\sigma$ Rydberg orbital constructed from $4p_z$ orbital on S and $3p_z$ orbital on O,

1δ : $3d\delta$ Rydberg orbital originated from $3d$ orbital on S.

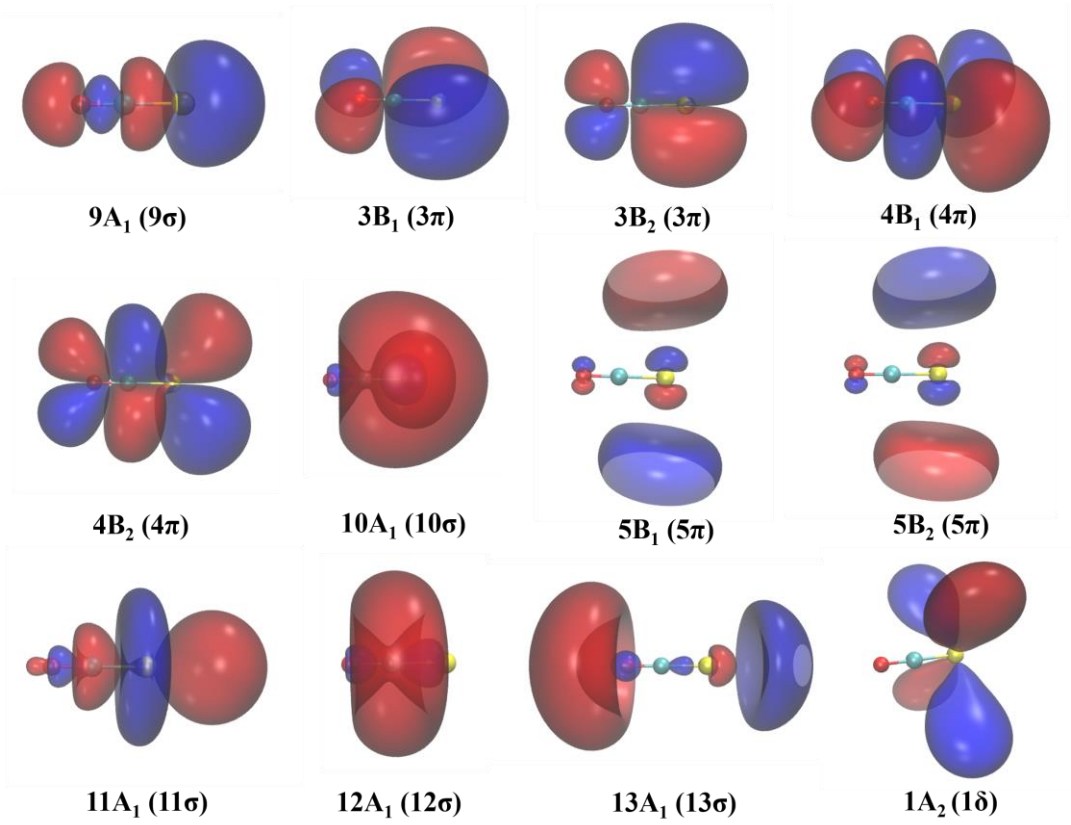

Figure S2. Relevant molecular orbitals that contribute to the electronic transitions of high-lying electronic states.

Table S1 summarizes our calculated vertical excitation energies (E_v) of various

singlet and triplet states up to 10 eV, compared with previous theoretical[14, 17] and experimental[13, 18 - 24] results. Spectroscopic assignments and features of the upper electronic states of OCS accessed in the present experiment (9~10 eV) have been hitherto controversial and rather unclear, due presumably to the quite complicated structures in the absorption spectrum and the lack of accurate ab initio calculations. In comparison to previous calculations,[14,17,25] a key difference here is that we include those Rydberg orbitals so that the Rydberg and mixed valence/Rydberg states in the energy range of interest can be captured. Given the incomplete information in various experiments, it should be noted in Table S1 that these experimental values lower than $2^1\Sigma^+$ state (~8.2 eV) are taken from the peak positions in the absorption spectra where they can be clearly identified, while those higher ones correspond to the reported 0_{00} bands of high-lying excited states. As a result, the calculated vertical excitation energies would not exactly correlate with the experimental absorption peaks due to the differences of equilibrium geometries and zero point energies between the ground and excited states, and the comparison is just used to assist the theoretical assignments.

Table S1 Calculated vertical excitation energies (in eV) of OCS compared to previous theoretical and experimental data. The energies are calculated in C_{2v} symmetry implemented in MOLPRO which only accepts an Abelian group. The lines in Bold correspond to the upper states that are directly probed at the experimental excitation wavelengths in this work

			Theory			Experiment							
$C_{\infty v}$	C_{2v}	C_S	[a]This work	[b]Ref. 17	[c]Ref. 14	Ref. 19	Ref. 13	Ref. 20	Ref. 21	Ref. 22	Ref. 18	Ref. 23	Ref. 24
$1^3\Sigma^+$	1^3A_1	$1^3A'$	5.019		5.050		4.900						
$1^3\Delta$	2^3A_1 1^3A_2	$2^3A'$ $1^3A''$	5.408		5.435								
$1^1\Sigma^-$	1^1A_2	$1^1A''$	5.649	5.662	5.730								
$1^3\Sigma^-$	2^3A_2	$2^3A''$	5.721		5.760								
$1^1\Delta$	2^1A_1 2^1A_2	$2^1A'$ $2^1A''$	5.731	5.743	5.850		5.550			5.580		5.504	5.506
$1^3\Pi$	1^3B_1 1^3B_2	$3^3A'$ $3^3A''$	7.102										
$1^1\Pi$	1^1B_1 1^1B_2	$3^1A'$ $3^1A''$	7.394		7.488		7.360			7.420	7.457	7.439	7.458
$2^3\Pi$	2^3B_1 2^3B_2	$4^3A'$ $4^3A''$	7.774				7.585				7.585 ($^3\Sigma^+$)		
$2^1\Pi$	2^1B_1 2^1B_2	$4^1A'$ $4^1A''$	8.326	8.392	8.400								
$2^1\Sigma^+$	3^1A_1	$5^1A'$	8.329	8.608	8.597		8.120			8.160	8.027	8.121	8.130
$2^3\Sigma^+$	3^3A_1	$5^3A'$	8.767										
$3^3\Pi$	3^3B_1	$6^3A'$	8.868			8.792	8.785	8.792	8.793	8.792	8.792	8.791	8.787

	3^3B_2	$5^3A''$		($E^1\Pi$)	($E^1\Pi$)	($E^1\Pi$)	($E^1\Pi$)	($4p\sigma^3\Pi$)	($4p\sigma^3\Pi$)	($4p\sigma^3\Pi$)	($E^1\Pi$)
$2^3\Delta$	4^3A_1 3^3A_2	$7^3A'$ $7^3A''$	8.872					8.788	8.788		
$2^1\Sigma^-$	3^1A_2	$5^1A''$	8.913								
$3^1\Pi$	**3^1B_1** **3^1B_2**	**$6^1A'$** **$6^1A''$**	**8.925**	**8.856** **($F^1\Pi$)**	**8.852** **($F^1\Pi$)**	**8.956** **($F^1\Pi$)**	**8.857** **($F^1\Pi$)**	**8.856** **($4p\sigma^1\Pi$)**	**8.856** **($4p\sigma^1\Pi$)**	**8.855** **($4p\sigma^1\Pi$)**	**8.850** **($F^1\Pi$)**
$2^1\Delta$	4^1A_1 4^1A_2	$7^1A'$ $7^1A''$	8.933				8.851	8.851	8.851		
$2^3\Sigma^-$	**4^3A_2**	**$6^3A''$**	**8.963**	**9.025** **(P)**	**9.023** **(P)**	**9.023** **(P)**			**9.023** **($4p\pi^3\Sigma^-$)**	**9.019** **($4p\pi^3\Sigma^-$)**	**9.017** **($P^1\Pi$)**
$3^1\Sigma^+$	5^1A_1	$8^1A'$	8.965	8.904			9.023 ($P^1\Sigma$)	9.023 ($4p\pi^1\Sigma^+$)			
$4^3\Pi$	4^3B_1 4^3B_2	$8^3A'$ $8^3A''$	9.508							9.462 ($5s\sigma^3\Pi$)	
$5^3\Pi$	5^3B_1 5^3B_2	$9^3A'$ $9^3A''$	9.548							9.468 ($3d\delta^3\Pi$)	
$4^1\Pi$	4^1B_1 4^1B_2	$9^1A'$ $8^1A''$	9.572							9.528 ($5s\sigma^1\Pi$)	
$5^1\Pi$	5^1B_1 5^1B_2	$10^1A'$ $9^1A''$	9.626						9.585	9.585 ($3d\delta^1\Pi$)	

[a]Franck-Condon transition at geometry with r = 1.165 Å, R = 2.245 Å, θ = 0°.

[b]Franck-Condon transition at geometry with r = 1.2 Å, R = 2.27 Å, θ = 0°.

[c]Franck-Condon transition at geometry with r = 1.164 Å, R = 2.223 Å, θ = 5°.

For low-lying excited states with $E_v < 8.0$ eV, our calculated energies and suggested assignments agree well with previous theoretical[14,17] and experimental[13,18,22-24] ones when available. For example, the $1^3\Sigma^+$, $1^1\Delta$ and $1^1\Pi$ states are calculated at 5.019, 5.731, and 7.394 eV in this work, which agree with the first three observed absorption band peaks within ~0.2 eV. [13,18,22-24] These states correspond to valence transitions and have already been well described by earlier calculations.[14,17] However, we find for the first time that a $2^3\Pi$ state at 7.774 eV which was observed in experiment by Leclerc et al.[13] and Cossart-Magos et al.[18] at ~7.5 eV, although the latter group assigned this state to be a $^3\Sigma^+$ state. Also, our calculated energy for the $2^1\Sigma^+$ state is 8.329 eV, which is closer to the experimental absorption peak at 8.027~8.160 eV,[13,18,22-24] compared to the previously calculated results at ~8.60 eV.[14,17] Furthermore, we find the $1^3\Pi$ and $2^1\Pi$ states at 7.102 and 8.326 eV, which have not yet been identified in experiments. Their absence in measured absorption spectra is possibly because the former is optically forbidden unless considering the spin-orbit coupling while the latter is hardly distinguishable with the $2^1\Sigma^+$ state. These results indicate that our calculations in this energy range are of the same or even better accuracy compared to previous ones with more inner orbitals included in the active space.[14,17]

Nevertheless, the assignments of diffused spectral bands above 8.5 eV are more difficult because of their Rydberg or mixed valance-Rydberg characters. Experimentally, Kopp[19] first identified three distinct progressions, originating from ~8.792, ~8.856, and ~9.025 eV, which were labelled as $E\ ^1\Pi$, $F\ ^1\Pi$, and P (unassigned) states, respectively. But he also warned that both E and F states could be assigned as

$^3\Pi$ states and *P*-*X* progressions possibly correspond to the same upper state as *F*-*X* bands.[19] These labels have been later followed by a variety of experimental groups.[13,20,21,24] Interestingly, Weinkauf et al.[21] and Limão-Vieira et al.[24] assigned the *P* state as having the $^1\Sigma$ and $^1\Pi$ symmetry respectively. However, Morgan et al.[22] attributed *E*, *F*, *P* states to Rydberg transitions from 3π to $4p\sigma$ (both *E* and *F*) and $4p\pi$ (*P*) orbitals, representing the $^3\Pi$, $^1\Pi$, and $^1\Sigma^+$ symmetry, respectively. Alternatively, according to an extremely high-resolution (~0.05 meV) absorption spectrum of jet-cooled OCS, Cossart-Magos et al.[18] proposed plausibly a more reliable set of assignments based on rotational lines, in which these three states were determined as $^3\Pi$, $^1\Pi$, and $^3\Sigma^-$ states generated by the same transitions analyzed by Morgan et al.[22]. Their assignments were later followed by Sunanda and coworkers[23]. In this work, we obtain three $^1\Pi$ states in this energy range from 8.326, 8.925, to 9.572 eV, which are inconsistent with earlier assignments in Refs.13,19-21,24. However, we do find a $^3\Pi$ state at 8.868 eV, with the dominant transition of $4p\sigma(13\sigma) \leftarrow 3\pi$, and a $^3\Sigma^-$ state at 8.963 eV, dominated by $4p\pi(5\pi) \leftarrow 3\pi$, very close to the $^1\Pi$ state at 8.925 eV, dominated by $4p\sigma(13\sigma) \leftarrow 3\pi$. Our results thus seem to support the assignments in Refs.18 and 23. On the basis of these analyses, we suggest that the tunable VUV laser in the present experiment prepares the vibrational states on the *F* $3^1\Pi$and *P* $2^3\Sigma^-$ states, respectively. The transition dipole moments from *X* $^1\Sigma^+$ to *F* $3^1\Pi$ is 0.358 a.u.. Schinke and coworkers have shown that spin-forbidden transitions of OCS can take place via strong spin-orbit couplings. For example, the spin-orbit corrected transition dipole moment from *X* $^1\Sigma^+$ to $1^3\Sigma^-$ is ~0.031 a.u., giving rise to the second large contribution

to the absorption spectrum among the lowest four excited states[14]. Here we estimated the transition dipole moment from $X\ ^1\Sigma^+$ to 6 ^{3}A" ($P\ 2^3\Sigma^-$) is 0.094 a.u., which supports the electronic transitions to these states.

Of course, many more Rydberg states in this high density region have been assigned in various experiments, we find some of them and attempt to offer plausible theoretical assignments correspondingly. For example, the $3^1\Sigma^+$ state, which was assigned by Weinkauf et al.[21] and Morgan et al.[22] as the *P* state, is found at 8.965 eV here, corresponding to $4p\pi(5\pi)/3p\pi(4\pi) \leftarrow 3\pi$ transition. The $2^3\Delta$ and $2^1\Delta$ states at 8.872 and 8.933 eV are in good agreement with the experimental levels at 8.788[18,22] and 8.851 eV[18,21,22], both corresponding to the transition of $4p\pi(5\pi) \leftarrow 3\pi$. Sunanda et al.[23] observed several spectral 0_{00} bands around 9.5 eV, such as $5s\sigma\,^3\Pi$, $3d\delta\,^3\Pi$, $5s\sigma\,^1\Pi$ and $3d\delta\,^1\Pi$ states, at ~9.462, ~9.468, ~9.528 and ~9.585 eV, respectively. We also find two $^3\Pi$ and two $^1\Pi$ states with the E_v at 9.508, 9.548, 9.572 to 9.626 eV, which have the same types of electronic transition. Furthermore, we find the $2^3\Sigma^+$ and $2^1\Sigma^-$ states at 8.767 and 8.913 eV, which have not yet been observed in any experiments. Overall, the agreement between theoretical and experimental energies and assignments of these high-lying electronic states is satisfactory. We have to note that a complete ab-initio determination of these high-lying Rydberg states converging to the ground state of OCS^+ with the current set up is impossible. In addition, the assignments for individual vibrational bands are impossible without having the semi-global potential energy surfaces. Both tasks are beyond the scope of this work.

Figure S3 depicts the adiabatic correlation diagram up to 10 eV for both SO + C

and CO + S products. The calculated energy threshold for the lowest SO($X\ ^3\Sigma^-$) + C(^{3}P) products with zero-point energy correction is ~8.725 eV, in line with the experimental estimate (~8.89 eV). It is noted that the SO($X\ ^3\Sigma^-$) + C(^{3}P) asymptote adiabatically correlates with the ground state $X\ ^1\Sigma^+$ of OCS, and three low-lying excited states, *i.e.*, $1^1\Pi$, $1^3\Sigma^+$ and $1^3\Pi$. The initial excited *E* ($3^3\Pi$), *F* ($3^1\Pi$), and *P* ($2^3\Sigma^-$) states adiabatically associate with the SO($^1\Delta$) + C(^{1}D) and SO($^3\Sigma^-$) + C(^{1}D) products lying above 10 eV. Thus, the production of SO($X\ ^3\Sigma^-$) + C(^{3}P) has to undergo complicated nonadiabatic pathways.

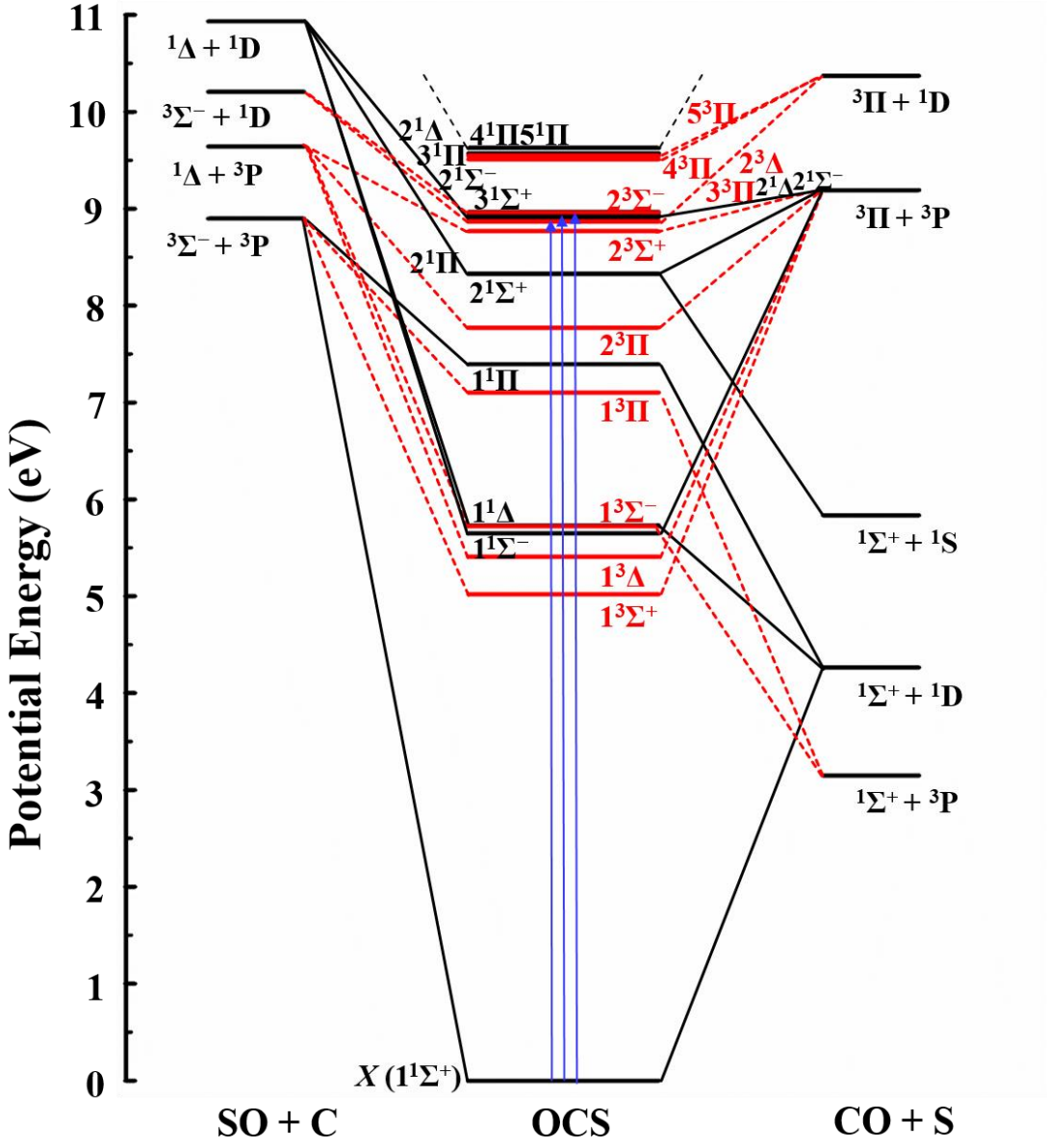

Figure S3. Adiabatic correlation diagram for OCS (in $C_{\infty v}$ symmetry) with the SO + C and CO + S products.

To seek the possible photochemistry mechanism, one typically follows the optimal deactivation pathway on the excited states from the Franck-Condon region to the product channel along the direction of gradient descent. This is however technically difficult for highly excited states which are quite close to and coupled with each other so that the geometry optimization on these states is a nontrivial task. Instead, we locate

several local minima at the ground state (X, $1^1A'$), whose energies and geometries are as given in Figure S4.

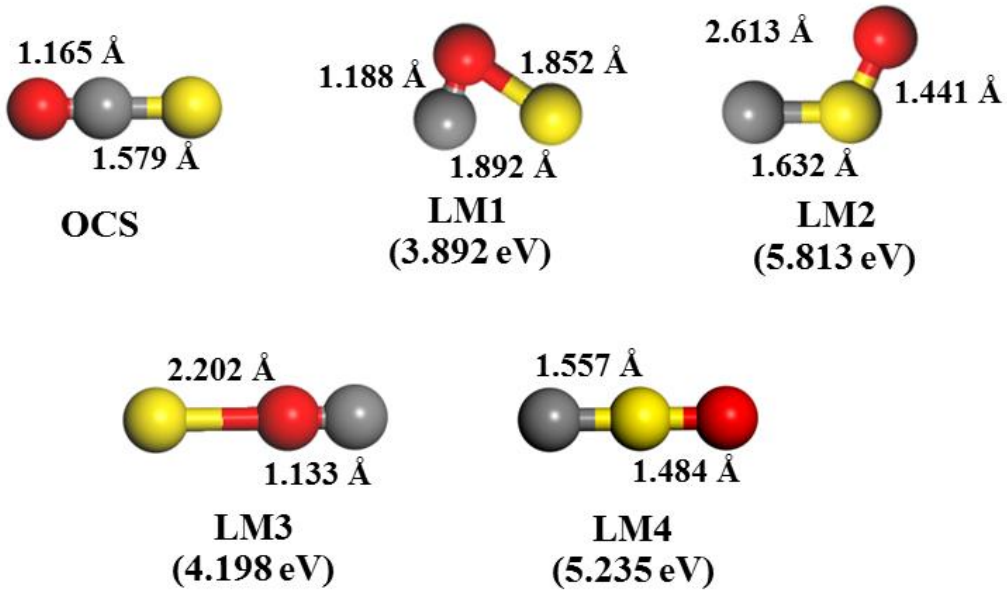

Figure S4. Geometries and energies of minima located at the electronically ground state.

Since only several low-lying states adiabatically correlate with the SO ($X\ ^3\Sigma^-$) + C (^{3}P) products, it is our beliefs that the OCS molecule is likely to dissociate going through these minima after fast conversions from the initial state to lower states. We therefore map out in Figure S5 that the potential energy curves of the lowest 12 singlet and 12 triplet states that are in the energy range of interest, along the pathway from OCS linear equilibrium to the SO ($X\ ^3\Sigma^-$) + C (^{3}P) limit via two bent local minima, as a function of the linearly interpolated internal coordinate (LIIC). We found that the dissociation pathway via LM3 and LM4 experiences a high barrier (>10 eV) that is inaccessible in our present experiment, which is thus not shown here. Note that collinear

Δ and Π states split into one A′ plus one A″ states in C_s symmetry while the molecule bends. As seen in Figure S5, one can see that the density of electronic states close to 9 eV near the Franck-Condon region is extremely high. These states feature shallow wells near the Franck-Condon region, which support numerous superimposed vibrational states bearing strong vibronic and/or spin-orbit couplings. The molecules excited to these vibrational states thus have a great chance to quickly make transitions to lower electronic states via internal conversions and/or intersystem crossings and then dissociate. We have discussed a representative pathway in the main text and one can easily find more pathways in Figure S5.

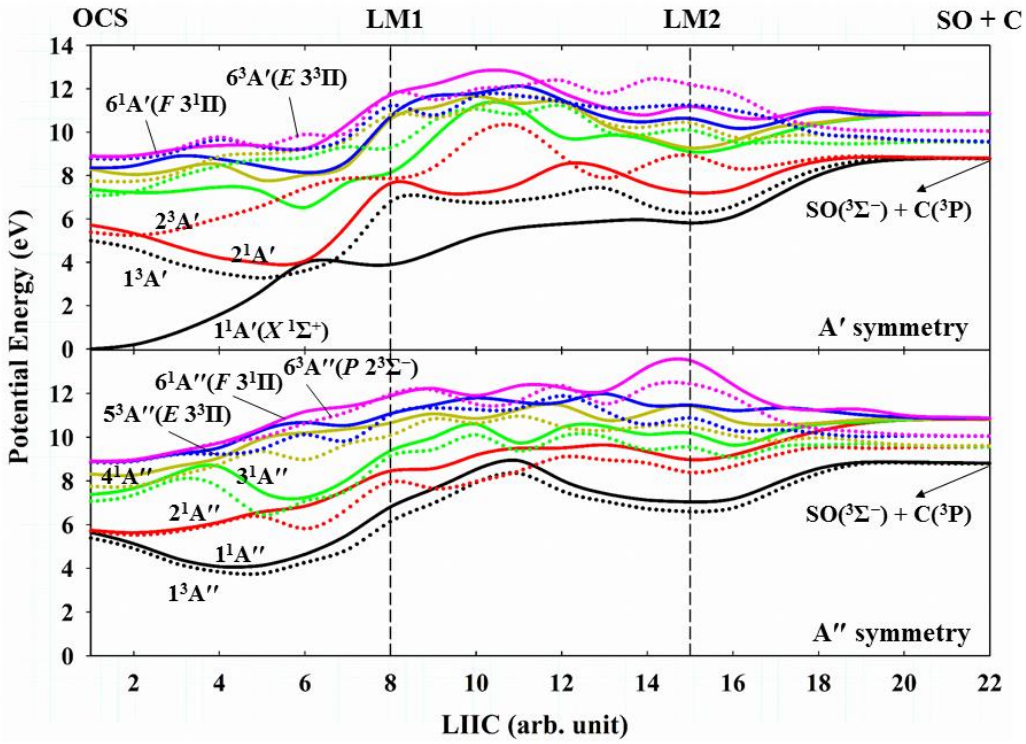

Figure S5. Potential energy curves of the lowest 12 singlet (solid curves) and 12 triplet (dotted curves) states in A′ (upper panel) and A″ (lower panel) symmetry along the linearly interpolated internal coordinates from the linear OCS equilibrium to SO + C products via two bent local minima (LM1 and LM2). Only the relevant states are labeled.

Regarding the roaming pathway, in Figure S6, we show that various CO + S channels are actually accessible in our experiment. Interestingly, the OCS molecule excited at these three long wavelengths is energetically quite close to the CO($^3\Pi$) + S(^{3}P) dissociation limit (~9.14 eV). In such cases, a molecule attempting to access this product channel could have insufficient energy to dissociate. The sulfur atom can be gradually pulled back by the long-range interaction between the CO + S fragments, followed by a long time of roaming and relaxation to the lower states, with the final intramolecular abstraction of the oxygen by the sulfur atom from the CO fragment. Indeed, the lower excited state a ($1^3A'$, $1^3\Sigma^+$), which adiabatically correlates with both the CO($^3\Pi$) + S(^{3}P) and SO ($X\ ^3\Sigma^-$) + C(^{3}P) products (see Figure S3), is rather flat in the asymptotic region so that the sulfur atom is very likely to roam back to the complex region via this state.

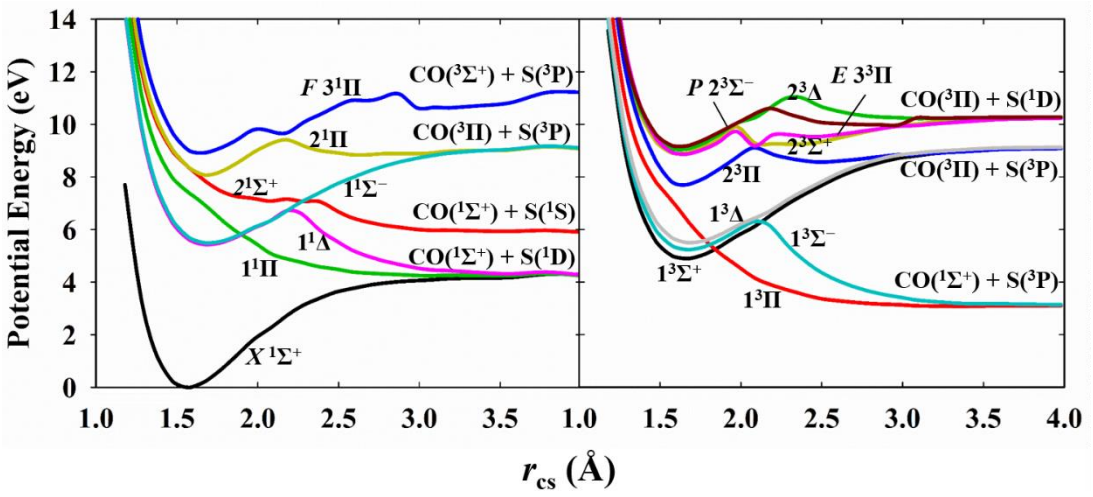

Figure S6. Potential energy curves of relevant singlet (left panel) and triplet (right panel) states in the linear geometry from the OCS equilibrium to CO + S products.

Since the S-C bond is weaker than the C-O bond, the S-C bond is more easily broken, followed by the roaming of S atom rather than C atom. For comparison, we calculate the dissociation limit of various O + CS channels as follows (see Table S2). It is clear that the OCS molecule excited at 138.53-134.57 nm would have energy that is higher than the CS ($^1\Sigma^+$) + O (^{1}D) dissociation limit (8.863 eV). This is different from the fact that the CO ($^3\Pi$) + S (^{3}P) limit has the energy of 9.14 eV. As a result, the OCS molecule excited at 138.53-134.57 nm has sufficient energy to dissociate to CS ($^1\Sigma^+$) + O (^{1}D) channel, which may not drive the roaming mechanism

Table S2. Dissociation energies of the CS+O channels.

CS + O channel	Dissociation energy (eV)
$^1\Sigma^+ + {}^3$P	6.877
$^1\Sigma^+ + {}^1$D	8.863
$^3\Pi + {}^3$P	10.262
$^3\Pi + {}^1$D	11.644

References

(1) Yu, S. R.; Yuan, D. F.; Chen, W. T.; Yang, X. M.; Wang, X. A. VUV Photodissociation Dynamics of Nitrous Oxide: The O($^1S_{J=0}$) and O($^3P_{J=2,1,0}$) Product Channels. *J. Phys. Chem. A* **2015**, *119*, 8090-8096.

(2) Yuan, D. F.; Yu, S. R.; Chen, W. T.; Ting, X.; Yang, X. M.; Wang, X. A. VUV Photodissociation Dynamics of Nitrous Oxide: The N($^2D_{J=3/2,5/2}$) and N($^2P_{J=1/2,3/2}$) Product Channels. *J. Phys. Chem. A* **2016**, *120*, 4966-4972.

(3) Yuan, D. F.; Yu, S. R.; Ting, X.; Chen, W. T.; Wang, S. W.; Tan, Y. X.; Wang, T.; Yuan, K. J.; Yang, X. M.; Wang, X. A. Photodissociation Dynamics of Nitrous Oxide near 145 nm: The O($^1S_0$) and O($^3P_{J=2,1,0}$) Product Channels. *J. Phys. Chem. A* **2018**, *122*, 2663-2669.

(4) Yu, S. R.; Yuan, D. F.; Chen, W. T.; Ting, X.; Wang, S. W.; Yang, X. M.; Wang, X. A. High-Resolution Experimental Study on Photodissociation of N_2O. *Chin. J. Chem. Phys.* **2016**, *29*, 135-139.

(5) Gao, H.; Song, Y.; Jackson, W. M.; Ng, C. Y. Communication: State-to-State Photodissociation Study by the Two-Color VUV-VUV Laser Pump-Probe Time-Slice Velocity-Map-Imaging-Photoion Method. *J. Chem. Phys.* **2013**, *138*, 191102.

(6) Werner, H.-J.; Knowles, P. J.; Knizia, G.; Manby, F. R.; Schütz, M. Molpro: a General-Purpose Quantum Chemistry Program Package. *Wiley Interdisciplinary Reviews: Computational Molecular Science* **2012**, *2*, 242-253.

(7) Knowles, P. J.; Werner, H. -J. An Efficient Method for the Evaluation of Coupling Coefficients in Configuration Interaction Calculations. *Chem. Phys. Lett.* **1988**, *145*, 514-522.

(8) Werner, H. -J.; Knowles, P. J. An Efficient Internally Contracted Multiconfiguration-Reference Configuration Interaction Method. *J. Chem. Phys.* **1988**, *89*, 5803-5814.

(9) Knowles, P. J.; Werner, H. -J. An Efficient Second-Order MC SCF Method for Long Configuration Expansions. *Chem. Phys. Lett.* **1985**, *115*, 259-267.

(10) Werner, H. -J.; Knowles, P. J. A Second Order Multiconfiguration SCF Procedure with Optimum Convergence. *J. Chem. Phys.* **1985**, *82*, 5053-5063.

(11) Langhoff, S. R.; Davidson, E. R. Configuration Interaction Calculations on the Nitrogen Molecule. *Int. J. Quant. Chem.* **1974**, *8*, 61-72.

(12) Hill, J. G.; Mazumder, S.; Peterson, K. A. Correlation Consistent Basisi Sets for Molecular Core-Valence Effects with Explicitly Correlated Wave Functions: The Atoms B-Ne and Al-Ar. *J. Chem. Phys.* **2010**, *132*, 054108.

(13) Leclerc, B.; Poulin, A.; Roy, D.; Hubin-Franskin, M. J.; Delwiche, J. Study of OCS by Electron Energy Loss Spectroscopy. *J. Chem. Phys.* **1981**, *75*, 5329-5348.

(14) Schmidt, J. A.; Johnson, M. S.; McBane, G. C.; Schinke, R. The Ultraviolet Spectrum of OCS from First Principles: Electronic Transitions, Vibrational Structure and Temperature Dependence. *J. Chem. Phys.* **2012**, *137*, 054313.

(15) Schmidt, J. A.; Johnson, M. S.; McBane, G. C.; Schinke, R. Communication: Multi-State Analysis of the OCS Ultraviolet Absorption Including Vibrational Structure. *J. Chem. Phys.* **2012**, *136*, 131101.

(16) Berning, A.; Schweizer, M.; Werner, H. J.; Knowles, P. J.; Palmier, P. Spin-Orbit Matrix Elements for Internally Contracted Multireference Configuration Interaction Wavefunctions. *Mol. Phys.* **2000**, *98*, 1823-1833.

(17) Danielache, S. O.; Nanbu, S.; Eskebjerg, C.; Johnson, M. S.; Yoshida, N. Carbonyl Sulfide Isotopologues: Ultraviolet Absorption Cross Sections and

Stratospheric Photolysis *J. Chem. Phys.* **2009**, *131*, 024307.
(18) Cossart-Magos, C.; Jungen, M.; Xu, R.; Launay, F. F. High Resolution Absorption Spectrum of Jet-Cooled OCS between 64000 and 91000 cm^{-1}. *J. Chem. Phys.* **2003**, *119*, 3219-3233.
(19) Kopp, I. On the Spectrum of OCS in the Vacuum Ultraviolet. *Can. J. Phys.* **1967**, *45*, 4011-4017.
(20) Yang, B.; Eslami, M. H.; Anderson, S. L. Multiphoton Ionization Photoelectron Spectroscopy Study of OCS-Rydberg Vibronic Structure and Ion State Selection. *J. Chem. Phys.* **1988**, *89*, 5527-5534.
(21) Weinkauf, R.; Boesl, U. Rydberg Spectroscopy of OCS: New Assignments in the 70000-74000 cm^{-1} Energy Region. *J. Chem. Phys.* **1993**, *98*, 4459-4470.
(22) Morgan, R. A.; Orr‐Ewing, A. J.; Ascenzi, D.; Ashfold, M. N. R.; Buma, W. J.; Scheper, C. R.; de Lange, C. A. Resonance Enhanced Multiphoton Ionization Spectroscopy of Carbonyl Sulphide. *J. Chem. Phys.* **1996**, *105*, 2141-2152.
(23) Sunanda, K.; Rajasekhar, B. N.; Saraswathy, P.; Jagatap, B. N. Photo-Absorption Studies on Carbonyl Sulphide in 30000–91000 cm^{-1} Region Using Synchrotron Radiation. *J. Quant. Spectrosc. Radiat. Transfer* **2012**, *113*, 58-66.
(24) Limao-Vieira, P.; Ferreira da Silva, F.; Almeida, D.; Hoshino, M.; Tanaka, H.; Mogi, D.; Tanioka, T.; Mason, N. J.; Hoffmann, S. V.; Hubin-Franskin, M. J.; Delwiche, J. Electronic Excitation of Carbonyl Sulphide (COS) by High-Resolution Vacuum Ultraviolet Photoabsorption and Electron-Impact Spectroscopy in the Energy Region from 4 to 11 eV *J. Chem. Phys.* **2015**, *142*, 064303.
(25) Suzuki, T.; Katayanagi, H.; Nanbu, S.; Aoyagi, M. Nonadiabatic Bending Dissociation in 16 Valence Electron System OCS. *J. Chem. Phys.* **1998**, *109*, 5778-5794.